Stony Brook University

Growth and characterization of $PbTiO_3/BaTiO_3$ superlattices

A Thesis Presented

by

Benedikt Ziegler

to

The Graduate School

in Partial Fulfillment of the Requirements

for the Degree of

Master of Arts

in

Physics

Stony Brook University

August 2009

Stony Brook University

The Graduate School

Benedikt Ziegler

We, the thesis committee for the above candidate for the Master of Arts degree, hereby recommend acceptance of this thesis.

Matthew Dawber – Thesis Advisor
Assistant Professor, Department of Physics and Astronomy

Peter Stephens – Chairperson of Defense
Professor, Department of Physics and Astronomy

Chris Jacobsen
Professor, Department of Physics and Astronomy

This thesis is accepted by the Graduate School.

Lawrence Martin
Dean of the Graduate School

Abstract of the Thesis

Growth and characterization of $PbTiO_3/BaTiO_3$ superlattices

by

Benedikt Ziegler

Master of Arts

in

Physics

Stony Brook University

2009

This thesis discusses the fabrication and characterization of $BaTiO_3$ thin films and $PbTiO_3/BaTiO_3$ superlattices. The samples were grown by an off-axis radio-frequency magnetron sputtering technique, layer-by-layer, in a new high vacuum chamber with a novel shutter design. The crystalline quality of the samples was determined by x-ray diffraction measurements. X-ray diffraction and low-angle x-ray reflection measurements were performed to determine the thickness of grown samples so that the growth rate could be determined. We performed surface roughness measurements with an atomic force microscope and could measure step-terrace structures of atomic flat samples.

We found a surprisingly large change of the lattice parameters for $BaTiO_3$ thin films with and without $SrRuO_3$ bottom electrodes ($c_{with} = 4.205\,\text{Å}$, $c_{without} = 4.095\,\text{Å}$). Furthermore the $BaTiO_3$ samples without an electrode were highly relaxed, whereas samples with an electrode were found to be almost coherent with the

(001) $SrTiO_3$ substrate. The influence of a $SrRuO_3$ electrode on $PbTiO_3$ thin films was not found to be nearly as big as for $BaTiO_3$.

Finally we grew coherent $PbTiO_3/BaTiO_3$ superlattices on (001) $SrTiO_3$ substrates at the growth condition for $PbTiO_3$. Growing superlattices with a lower $PbTiO_3$ concentration than 50 % turned out to be difficult due to the non-optimal growth condition for $BaTiO_3$. The c/a ratio of our samples was measured and compared to the theoretical calculations.

Contents

List of Figures

List of Tables

Acknowledgements

I like to express my gratitude to my supervisor Professor Matthew Dawber for his invaluable assistance, support and guidance. My thanks goes also to John Sinsheimer and Sara Callori for their support and for reading the manuscript of this thesis.

I would also thank the *German Academic Exchange Service* (DAAD) for the opportunity to write this master thesis in the United States and for the nine month of funding.

Special thanks goes to my friends in Neustadt, Würzburg and Stony Brook who always have been there for me.

And I want to express my love and gratitude to my beloved family; for their understanding, support, and love, through the duration of my studies.

Chapter 1

Introduction

The ferroelectric effect was first observed in Rochelle salt in 1921 [1]. The first ferroelectric materials had a complex lattice structure and the physical understanding was very limited until the simpler ferroelectric perovskite $BaTiO_3$ was discovered in 1945 [2]. Since then the ferroelectric effect has been better understood and nowadays ferroelectric materials are widely used in many different devices, often for their pyroelectric and piezoelectric properties. Interesting examples are non volatile memories, ferroelectric Random Access Memories (RAM), thermal infrared pyroelectric detectors, miniature electromechanical devices or ultrasonic sensors.

The perovskite ferroelectric materials, with the chemical formula ABO_3, are well studied because of their simple crystalline structure. Two of the most studied examples of ferroelectric perovskites are $PbTiO_3$ and $BaTiO_3$.

Modern growth techniques allow growth of epitaxial ferroelectric thin films with different strains or artificial materials with novel properties. In recent work, where the ferroelectric properties of $BaTiO_3$ thin films were modified, the spontaneous polarization was enhanced to about 270 % of the bulk value [3]. Another advantage of these growth techniques is the ability to grow one-unit-cell thick layers and thereby, layer-by-layer, artificial structures of different components with different properties. These new materials have properties which are a mixture of properties of the base materials, like $BaTiO_3/SrTiO_3$ superlattices which have an enhanced spontaneous polarization due to the strained $BaTiO_3$ [4], or can even have completely new behaviors like $PbTiO_3/SrTiO_3$ superlattices, which exhibit a recovery of ferroelectricity for ultra thin superlattice periods [5], [6]. Recent theoretical calculations predict the enhancement of the piezoelectric effect in $PbTiO_3/BaTiO_3$ superlattices due to the different polarization-strain coupling in $PbTiO_3$ and $BaTiO_3$.

In this work, I will show how we have overcome the experimental challenges

to grow thin film $BaTiO_3$ and $PbTiO_3/BaTiO_3$ superlattices.

Chapter 2

Background

Ferroelectric behavior was first discovered in Rochelle salt, a hydrogen-bonded material (1921) [1]. Ferroelectric materials have a switchable spontaneous polarization and are also pyroelectric and piezoelectric. The physical understanding of ferroelectricity changed when it was discovered in the non hydrogen containing, perovskite oxide $BaTiO_3$ in 1945 [2]. The perovskites have a much simpler structure which allows a better understanding of the origins of ferroelectricity. In this chapter, we will discuss the perovskite ferroelectrics and the phenomenological Landau-Devonshire theory which describes the macroscopic properties.

2.1 Perovskite oxides

The perovskite structure has its name from the $CaTiO_3$ crystal, which was found in the Ural mountain (Russia) and was named after the Russian mineralogist L.A. Perovski (1792-1856). The compound has a pseudo-cubic structure with five atoms in its unit cell (ABO_3). It has an A atom on each corner of the cube, a B atom in the center and an oxygen atom on each face, which together build an oxygen octahedron around the B atom (see Fig. 2.1). The A and B atoms are cation elements or a mixture of two or more elements (e.g. $PbTi_{1-x}Zr_xO_3$). The valence of the A cation ranges from +1 to +3 and the one from the B cation ranges from +3 to +6. Depending on the components, the perovskite oxides can have very different properties: they can be insulating (para-, ferroelectric, (anti)ferromagnetic, multiferroic), conducting (metallic with or without (anti)ferromagnetic order) or superconducting.

The ideal perovskite structure has a high symmetry reference structure which is for most the ferroelectric perovskite oxides the high temperature paraelectric phase. This state is usually in the $Pm\bar{3}m$ space group. With

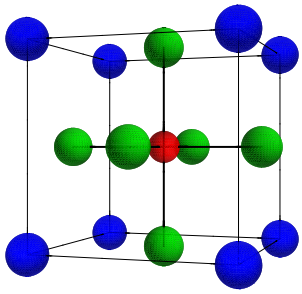

Figure 2.1: The cubic perovskite structure with an A atom (color) on each corner, one B atom (color) in the center and the oxygen octahedron.

decreasing temperature the perovskite structure undergoes one or more structural phase transitions which lower the symmetry of the structure and create a ferroelectric phase. The number of phase transitions can be different for each material and depends on the composition of the material and the hybridization of the atomic orbitals.

In the ferroelectric phase, the materials have two or more stable or metastable states with a nonzero polarization in zero external electric field. This is called a spontaneous polarization and the direction can be switched with an external electric field. The direction of the spontaneous polarization is defined when a bulk ferroelectric material undergoes the ferroelectric phase transition. This direction can be in any of the six possible directions in the case of an transition of a cubic to a tetragonal structure. However, in thin films and superlattices the direction of the spontaneous polarization may be pinned by the lattice mismatch between the different materials and the substrate.

Regions with the same direction of polarization are called *ferroelectric domains* and the area between regions of different polarizations are called *domain walls*. The size and orientation of domains depend on the electrical and mechanical boundary conditions. Like ferromagnetic materials, ferroelectric materials have a hysteresis loop which can be recorded as a polarization-electric field loop (PE). Fig. 2.2 shows the PE loop of a Samsung $Pb(Zr,Ti)O_3$ sample. For a sample with zero polarization (*i.e.*, a 50/50 balance of oppositely poled domains), the curve starts at the origin (1). With an increasing external applied electrical field E the domain walls start moving. Domains with orientation in direction of the applied field will grow and new domains can nucleate. The polarization is saturated when all domains are aligned with the external field (2). The increase in polarization for stronger fields is due to the dielectric charging (3). When the electric field is lowered the domains will

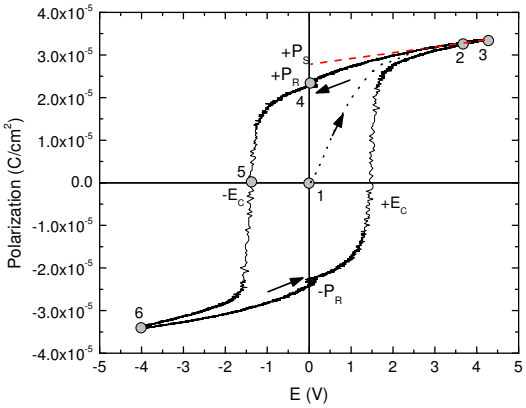

Figure 2.2: Polarization-electric field loop shows the switching of the polarization between the two states for a $Pb(Zr,Ti)O_3$ Samsung sample.

stay polarized in the same direction and the polarization will decrease but it will be non zero at zero applied field (4). This remaining polarization is called *remanent polarization* $+P_R$. If the electric field is increased in the opposite direction (negative voltage) the polarization will decrease further and will suddently switch at the field $-E_C$ which is called *coercive field*. The domains will grow and the polarization will saturate (6). Decreasing the field to zero voltage will lower the polarization to the value $-P_R$ for $E = 0$ V. Increasing the field in the opposite direction will give the value for $+E_C$ where the polarization suddently switches. The *spontaneous polarization* $+P_S$ is defined by the linear extrapolation of the high field (saturated region) to zero field.

2.1.1 A- and B-site driven ferroelectrics

In this work we are particularly interested in $BaTiO_3$ and $PbTiO_3$ which have different behaviors driving the ferroelectricity. Goldschmidt (1926) introduced two rules for the perfect perovskite structure which give an ideal relationship between the ionic radii. The deviation from this ideal perovskite structure can be measured with the tolerance factor t which is defined as $t = (r_A + r_O)/\sqrt{2}\,(r_B + r_O)$ where r_A and r_B are the ionic radii of the cations and r_O is the ionic radius of the anions. For $t \approx 1$ the perovskite structure is formed. In our case the B-site is always occupied by an Ti atom which implies that t is only depending on the ionic radius of the A-site cations. For $t > 1$, the structure is dominated by the A-O distance and the titanium atom in the B-site is too small for the oxygen octahedron. This allows the Ti atom to move off center and creates an polar distortion. These kind of materials are

called *B-site driven* (*e.g.*, $BaTiO_3$). When $t < 1$ the materials are called *A-site driven* and are often not ferroelectric. The A-site cation is too small for the hole between the oxygen octahedra and a distortion (tilt or rotation) of the oxygen octahedra is favored (e.g. $SrTiO_3$ or $CaTiO_3$).

In the case of $PbTiO_3$ the $6s$ states of the Pb^{2+} hybridize with the O $2p$ states which leads to a large strain that stabilizes the tetragonal phase. This *Pb-O* hybridization also has an indirect effect on the *Ti-O* hybridization which is necessary for ferroelectricity [7].

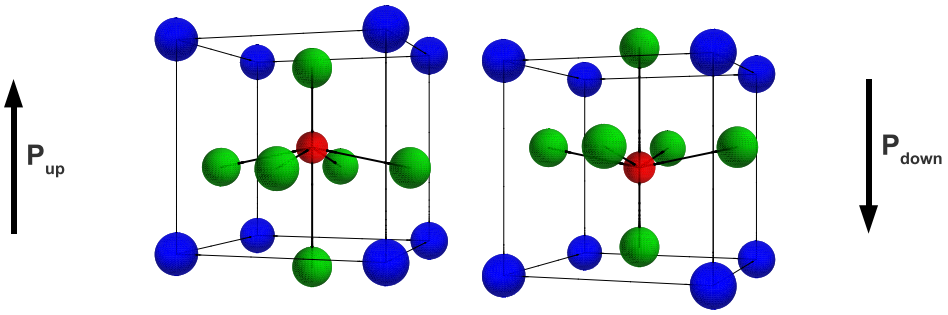

Figure 2.3: Perovskite structure with a displacement of the oxygen octahedra and the B-site cation with respect to the lead atom which corresponds in a spontaneous polarization up and down

2.2 Landau-Devonshire Theory

The Landau Theory for phase transitions was first applied to ferroelectrics by Devonshire. This section will discuss the Landau-Devonshire approach to explain the macroscopical phenomena of ferroelectrics. For a more detailed explanation, the reader is referred to [8] and [9].

The basic idea is to expand a thermodynamic polynomial potential as a function of the dependent variables. A suitable potential is the elastic Gibbs free energy, G, which is a function of temperature, stress, and displacement. The simplest case assumes that all stresses are zero, that the direction of the displacement is along a crystallographic axes (i.e. that the spontaneous polarization and the external electrical field are directed along the same axes), and that the non-polar phase is centrosymmetric. In this approximation and in the vicinity of a phase transition, the free energy can be expanded in powers

of the polarization P

$$G = \frac{\alpha}{2}P^2 + \frac{\gamma}{4}P^4 + \frac{\delta}{6}P^6 - EP \tag{2.1}$$

where E is the electric field and α, γ, and δ are coefficients. The equilibrium configuration can be found by finding the minima of G:

$$\frac{\partial G}{\partial P} = \alpha P + \gamma P^3 + \delta P^5 - E = 0 \tag{2.2}$$

$$E = \alpha P + \gamma P^3 + \delta P^5. \tag{2.3}$$

The Landau-Devonshire theory assumes that only the coefficient α is temperature dependent. For a temperature close to the transition temperature T_0, α is assumed to be linearly in temperature: $\alpha = \beta\,(T - T_0)$ where β is positive. The other coefficients are assumed to be independent of the temperature. The order of the transition depends now on the sign of γ (first order $\gamma < 0$, second order $\gamma > 0$) and δ is necessarily positive ($\delta < 0$, $\lim_{P\to\infty} U = -\infty$). In the following, the two different kinds of transitions are described.

2.2.1 First-order (discontinuous) transition

For the case of $\gamma < 0$ in Eq. 2.1 we have a first-order transition. The Curie temperature T_C is defined by the conditions $G = 0$ and $\frac{\partial G}{\partial P} = 0$ for $P \neq 0$ in a zero external field ($E = 0$). With this conditions and Eq. 2.3 we obtain:

$$0 = \frac{\beta}{2}\,(T - T_0)\,P^2 + \frac{\gamma}{4}P^4 + \frac{\delta}{6}P^6 \tag{2.4}$$

$$0 = \beta\,(T - T_0)\,P + \gamma P^3 + \delta P^5 \tag{2.5}$$

From this equation system we obtain with $T = T_C$ and $P \neq 0$:

$$T_C = T_0 + \frac{3}{16}\frac{\gamma^2}{\beta\delta} \tag{2.6}$$

This result implies that the Curie temperature is higher than the transition temperature and that there are minima in the free energy potential even for $T > T_0$ at non-zero polarization (see Fig. 2.4). For the temperature $T = T_0$ there are two stable states at $P \neq 0$. These minima correspond to the spontianeous polarization P_S. The temperature dependence of P_S can be determined

by solving the second equation of Eq. 2.5 and by using Eq. 2.6:

$$P_S^2(T) = \frac{\gamma + \sqrt{\gamma^2 + 4\beta\delta(T_0 - T)}}{2\delta} \tag{2.7}$$

$$P_S^2(T_C) = \frac{3\gamma}{4\delta} \tag{2.8}$$

For $T > T_C$ is $P_S = 0$ but it jumps to the value $\sqrt{\frac{3\gamma}{4\delta}}$ when $T = T_C$. This phase transition behavior is called a first-order or discontinuous transition.

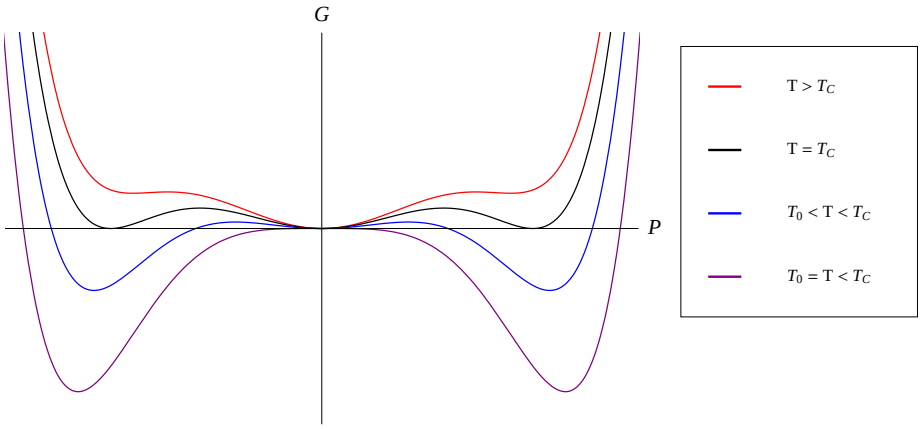

Figure 2.4: Free energy potential G vs. the polarization P for a first-order transition with the transition temperature T_0 and the Curie-Weis temperature T_C

2.2.2 Second-order (continuous) transition

The second-order transition occurs when $\gamma > 0$ in Eq. 2.1. In this case we can neglect the higher orders in P and can write:

$$\frac{\partial G}{\partial P} = \beta(T - T_0)P + \gamma P^3 = 0 \tag{2.9}$$

This equation has one solution ($P = 0$) for $\alpha > 0$ and two solutions ($P \neq 0$) for $\alpha < 0$. The transition occurs therefore at $\alpha = 0$ and $T = T_0 = T_C$. The temperature dependence of P_S can be determined from Eq. 2.9 with $P \neq 0$:

$$P_S^2(T) = \frac{\beta}{\gamma}(T_C - T), \quad P_S \to 0 \tag{2.10}$$

We see that P_S undergoes a continuous transition at T_C. The precision of the equation is limited to small values of P_S due to the polynomial approximation.

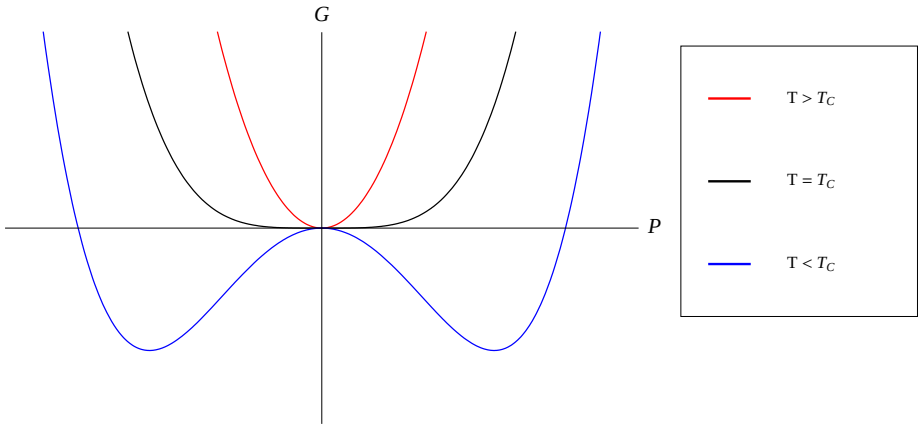

Figure 2.5: Free energy potential G vs. the polarization P for a second-order transition where $T_0 = T_C$

Chapter 3

Materials

3.1 Ferroelectric materials

3.1.1 $PbTiO_3$

$PbTiO_3$ has a first-order transition at $T_c = 493\,°C$ from a cubic paraelectric to a tetragonal ferroelectric phase ($a = b = 3.904\,Å$, $c = 4.152\,Å$). $PbTiO_3$ is a classical example for a displacive ferroelectric transition. The oxygen octahedra and the B site cation are displaced with respect to the A site cation. The direction of the displacement is the same but the magnitude for the oxygen atoms is larger than for the titanate atom. This difference in the center of mass of the positive ions (lead and titanate) to the center of mass of the oxygen octahedra creates a net dipole moment per unit cell, or polarization. The behavior that the octahedra and the B site cation have a displacement in the same direction is a feature of an A-site driven ferroelectric material. This textbook like behavior of a displacive ferroelectric transition is due to the hybridization of the lead and oxygen states, leading to a large strain which stabilizes the tetragonal phase [7]. $PbTiO_3$ shows the normal double well potential for the free energy G for $T < T_C$. The spontaneous polarization can be as high as $75\,\mu C/cm^2$ [8]. The lattice mismatch of the in-plane lattice parameter between $PbTiO_3$ and (001) $SrTiO_3$ is $0.02\,\%$.

3.1.2 $BaTiO_3$

$BaTiO_3$ is a paraelectric ferroelectric with a cubic perovskite structure ($m3m$) above $120\,°C$ ($a = b = c = 4.01\,Å$). In contrast to $PbTiO_3$ it has three ferroelectric phase transitions below $120\,°C$: first to tetragonal ($4mm$) ($a = b = 3.99\,Å$, $c = 4.04\,Å$), then to orthorhombic (mm) below $T \approx -3\,°C$ ($a = 4.01\,Å$, $c = 3.98\,Å$), and finally to a trigonal phase ($3m$) at $T = -93\,°C$ ($a = 4.00\,Å$).

The polar axes in the three ferroelectric phases are [001], [011], and [111] respectively [10]. The reason for these extra phase transitions of $BaTiO_3$, compared to the one of $PbTiO_3$ is the completely ionic interaction between barium and oxygen which favors a rhombohedral structure [7]. The spontaneous polarization of single crystal $BaTiO_3$ is $26\,\mu C/cm^2$ [11]. By strain engineering it was shown that the spontaneous polarization can be enhanced up to $70\,\mu C/cm^2$ on (110) $DyScO_3$ (strain $\epsilon_S = -1.3\,\%$) [3].

3.2 $SrRuO_3$ Electrodes

$SrRuO_3$ is a metallic perovskite compound with an orthorhombic structure with $a = 5.53\,Å$, $b = 5.57\,Å$and $c = 7.85\,Å$which becomes ferromagnetic below $155K$. It has a lattice distortion of $89.6\,°$ between [110] and [$\bar{1}$10] in the (001) plane. The structure can be seen as pseudo-cubic with $a = b = c = 3.93\,Å$which results in a very small in-plane lattice mismatch between $SrRuO_3$ and $SrTiO_3$ (0.64 %) [12]. $SrRuO_3$ can be grown in very high quality with an

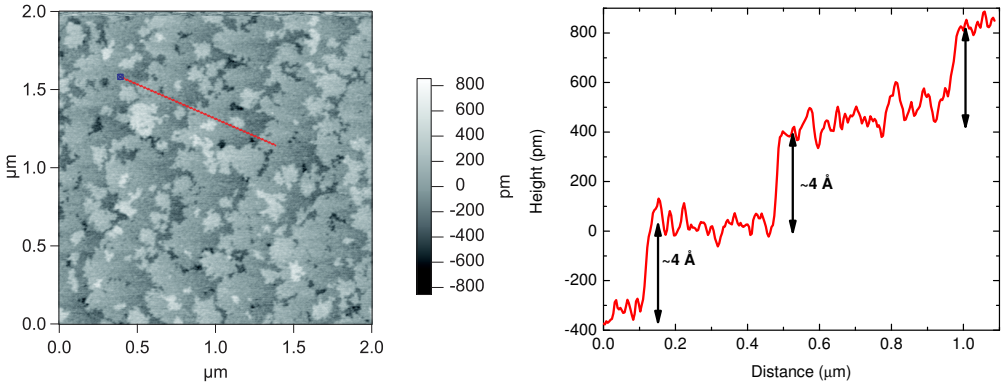

(a) (b)

Figure 3.1: (a) Atomic force microscope image of an atomically flat surface with step-terrace structure of a $SrRuO_3$ film on (001) $SrTiO_3$ substrate (Technique is explained in Chap. 5.3.1). The red line indicates the cut height profile shown in (b). The step size is one unit cell ($\sim 4\,Å$)

atomically flat surface (see Fig.3.1) on TiO_2 terminated $SrTiO_3$ substrates. In [13], it was shown that the choice of the electrode material can have a big influence on the coercive field and the remanent polarization due to parasitic capacitance at the interface between electrode and thin film. These effects are minimized by the use of $SrRuO_3$ bottom and top electrodes. The other advantage of using $SrRuO_3$ as an top electrode is the *in-situ* growth which

prevents the sample from contamination which can occur from the contact with air.

3.3 $SrTiO_3$

$SrTiO_3$ is paraelectric and has a cubic perovskite structure ($a = b = c = 3.905\,\text{Å}$) at room temperature. The crystal structure becomes tetragonal ($c/a = 1.00056$) at a transition temperature of 105 K but does not become ferroelectric in a bulk material. It has been shown that strain engineering can induce ferroelectricity in $SrTiO_3$ at room temperature [14]. We use TiO_2 terminated $SrTiO_3$ as a substrate since it has a relativly small lattice mismatch with the in-plane lattice parameters of $PbTiO_3$ ($< 0.1\,\%$) and $SrRuO_3$ ($0.6\,\%$). However, the lattice mismatch with $BaTiO_3$ is $2.2\,\%$ which makes it harder to grow $BaTiO_3$ films on $SrTiO_3$ substrates. Crucially in the case of both $PbTiO_3$ and $BaTiO_3$ use of $SrTiO_3$ substrates ensures that the polarization is directed out-of-plane, which is the easiest direction to probe using our measurement techniques.

Chapter 4

Sample preparation

4.1 RF sputtering

For the growth of epitaxial oxide films different techniques can be used. Usually a single crystal substrate which has a good matching between its lattice constants and the ones of the film material is used. Growth techniques like pulsed laser deposition, sputtering or molecular beam epitaxy (MBE) all fall within the group of *physical vapor deposition techniques*. Since we are using the sputtering technique it is described here briefly. For a more detailed description of the different techniques the reader is referred to [9].

The ferroelectric thin films and superlattices are grown with RF off-axis sputtering. This technique removes atoms from the surface of a ceramic target with highly energetic argon ions. The kinetic energy is transfered from argon ions to the target surface atoms. In this process the stochiometrical composition of the target material is obtained in the growing film. This is an advantage in the growth of complex oxides when compared to MBE or evaporation methods. On the other hand, although it is more difficult, MBE does allow a higher degree of control over complex oxide interfaces.

An rf field with a frequency of 13.56 MHz between the cathode (sputter gun) and the anode (substrate and rest of the chamber) produces plasma from argon gas in front of the target. The plasma is held in place by a magnetic field produced by strong permanent magnets behind the target (see Fig. 4.1). Only the electrons in the plasma are light enough to response to high frequency of the rf field. The smaller size of the cathode (target) compared to the anode results in a higher electron concentration in front of the cathode which produces a negative dc bias. This self-bias is responsible for the acceleration of the argon ions towards the target which causes the sputtering of the target surface atoms. The ejected atoms from the target reach the substrate and build a film

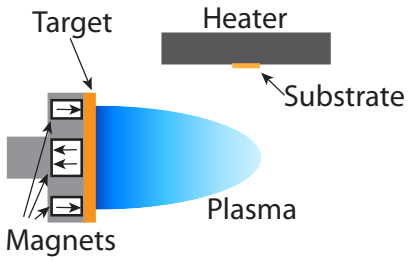

Figure 4.1: Geometry of the off-axis rf sputtering technique.

on top. Depending on the material an additional oxygen flow is supplied into the chamber to keep the film oxidized. Since the target for complex oxides like perovskite ferroelectrics is a multielement source and every element has a different sputtering yield due to the differences in the atomic mass and the chemical bonding environment it is necessary to perform a "presputtering" for every target material and for each change of growth parameter. During the presputtering the content of elements which sputter more easily are reduced on the surface and a higher ratio of the elements which are removed harder stays behind. The presputtering thereby ensures an equilibrium of the stochiometrical composition on the surface of the target.

4.2 Shutter design

Since one of the major fields of research in our group is the growth of different kinds of superlattices, we use a growth chamber with six rf sputter guns. When compared to more commonly used setups with three or four guns, this high number of guns allows the growth of different kinds of superlattices without changing the target material, the growth of tricolor superlattices with electrodes, or the growth of different bottom and top electrodes. This bigger variety of experimental options increases the complexity of the chamber geometry. The geometry of the guns can be seen in Fig. 4.2. The guns were fit as close as possible around the center of the chamber to increase the growth rate. This geometry made it impossible to use the standard design for the gun shutters where the shutters rotate in front of the guns from the side. In our chamber the shutters have a U shape and slide in from below the guns as can be seen in Fig. 4.2.

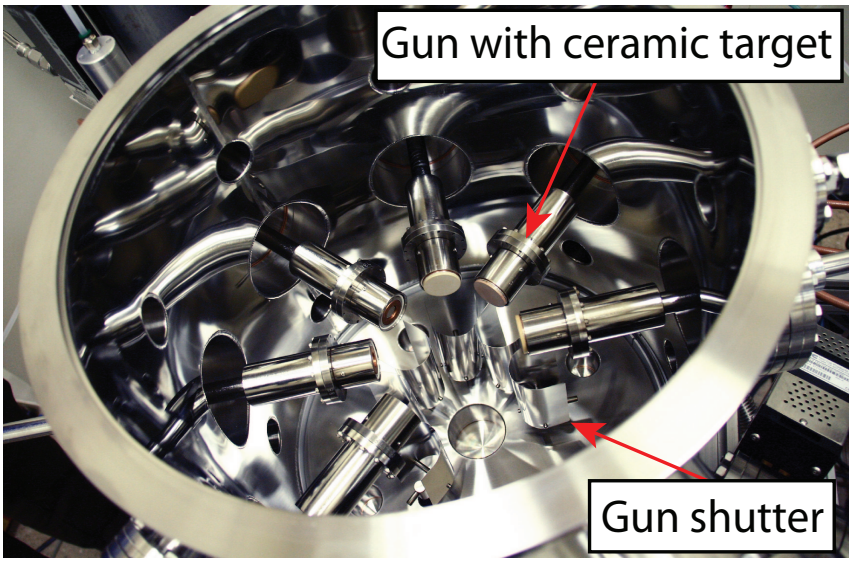

Figure 4.2: Geometry of the six rf sputter guns around the center of the chamber

4.3 Growth conditions

The growth conditions for different materials are strongly dependent on their containing elements. For example, the Pb in $PbTiO_3$ is very volatile, which does not allow a very high growth temperature, unlike $BaTiO_3$ which can be grown at very high temperatures. The gas pressure and ratio also have a big influence on the quality of the film and the growth rate of the material. Furthermore, the geometry of the vacuum chamber can affect the conditions, mainly the growth rate. We list in table 4.1 the different growth conditions which were used to grow the thin films and the superlattices. The growth

Material	Temperature	Pressure	Flow O/Ar
BTO	650	40	4/16
PTO	540	180	7/16
PTO/BTO	550	180	7/16
SRO	600	100	6/32

Table 4.1: Growth parameter for $BaTiO_3$, $PbTiO_3$, $SrRuO_3$ and the $PbTiO_3/BaTiO_3$ superlattices. The temperatures are given in °C, the pressure in mTorr, and the flow rates in sccm.

conditions for $PbTiO_3$ and $SrRuO_3$ were adopted from previous work in a similar chamber [5].

4.4 Sample wiring

To measure the piezoelectric properties of the samples, we need to wire the bottom electrodes to the AFM sample stub to get a good ground. We used therefore a commercial bonding machine which punches a wire through the ferroelectric film with ultrasonic frequencies allowing contact with the underlying $SrRuO_3$ electrode (see Fig. 4.3).

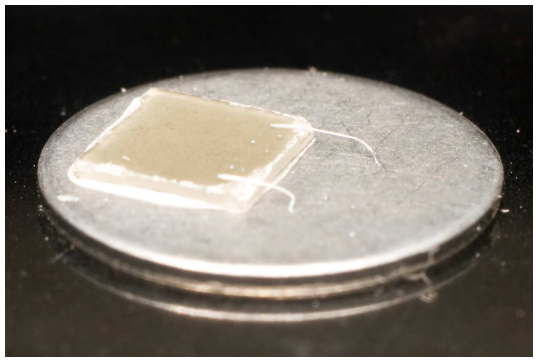

Figure 4.3: $SrRuO_3$ bottom electrode is wire-bonded to a AFM sample stub

Chapter 5

Techniques

We used different techniques for the structural characterization of the thin films and superlattices. The most important one is x-ray diffraction, which is used to determine the lattice constants of the film or the superlattice. It was also used to determine the thickness of the sample and was compared to the thickness measurements from low angle x-ray reflection scans. Atomic force microscopy was performed to measure the substrate and film roughnesses, and piezoresponse force mircroscopy was used to varify the ferroelectricity of our samples.

5.1 X-ray diffraction

For the x-ray measurements we used a high resolution diffractometer *Bruker D8 Discover*. It is equipped with a Göbel mirror and a two-bounce Ge(222)

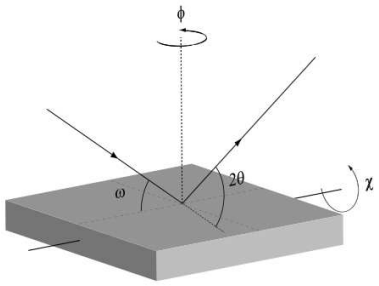

Figure 5.1: The schematic shows the four angles (ω, 2θ, ϕ, χ) of a four circle diffractometer

monochrometer at the incident beam and a variable slit or a triple bounce

analyzer at the diffracted beam. For the measurement of the rocking curves, θ-2θ scans, reflectivity curves and reciprocal space maps we used copper $K\alpha_1$ radiation. In Fig. 5.1 are the four angles (ω, 2θ, ϕ, χ) of the typical four circle diffractometer shown. The two angles (ξ, ζ) of the tilting stage (not shown in the figure) allow us to align the sample normal parallel to the ϕ axis of the diffractometer. This alignment gives access to the full reciprocal lattice with $\omega = \phi$.

5.1.1 Rocking curve

A rocking curve is a scan in ω with fixed 2θ angle. The measurement is performed to determine the offset angle in ω or to measure the quality of the substrate and the film. Any structural defect will broaden the peak or will even

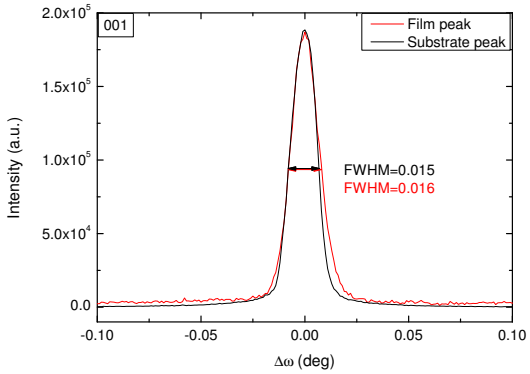

Figure 5.2: The diagram shows the rocking curves with FWHM of the film ($BaTiO_3$) and the substrate ($SrTiO_3$)

create multiple peaks. The crystallinity of sample can be determined by the full width at half maximum (FWHM). For an epitaxial growth of the film on top of the substrate, the FWHM of the film and substrate should be of equal value. The FWHM depends on the optic which implies that a comparison of the film FWHM and the substrate FWHM gives a better indication of the sample than each scan taken by its own. In Fig. 5.2, the two rocking curves of the film and the substrate of an $BaTiO_3$ film are shown. The almost equal FWHM of substrate (0.015°) and film (0.016°) indicates the epitaxial growth of the film.

5.1.2 θ-2θ scans

θ-2θ scans are performed to determine the interplane distance d. d is determined from the measured angle by using Bragg's law

$$2d \sin\theta_n = n\lambda \tag{5.1}$$

where n is the order of diffraction and $\lambda = 1.5402\,\text{Å}$is the wavelength of the Cu $K\alpha_1$ radiation. The Bragg plane is selected by choosing the appropriate ϕ and χ angle.

In thin films, the finite number of planes produce oscillations in the intensity close to the diffraction peak. The number of planes and therefore the thickness of the film can be determined by these oscillations.

A simple kinematical approach can be used to fit a curve to the experimental data. We are using a code written in *MatLab*© to simulate the diffracted intensity for singel layers and superlattices (see Appendix A). The *structure factor* S_{el} for the elementary unit cell is calculated in the classical model by

$$S_{el}(\mathbf{K}) = \sum_{j=1}^{n} f_j(\mathbf{K})\, \mathbf{e}^{\mathbf{iK}\cdot\mathbf{d_j}}, \tag{5.2}$$

where f_j is the *atomic form factor* which is approximated by a polynomial series, $\mathbf{K}$ is the wave vector and $\mathbf{d_j}$ are the base vectors for the atoms. The thickness of one layer is taken into account by a structure factor of the crystal S_c:

$$S_c(\mathbf{K}) = S_{el} \cdot \frac{\sin(\mathbf{K}\cdot\mathbf{d_j}\cdot N)}{\sin(\mathbf{K}\cdot\mathbf{d_j})} \tag{5.3}$$

where N is the number of unit cells per layer. Fig. 5.3 shows a θ-2θ diffractogram of a $BaTiO_3$ film around the (001) peak of the $SrTiO_3$ substrate. Since our films are usually growing with an orientation of the c-axis perpendicular to the (001) plane, we can determine the c-axis value from the film peak position. For the $BaTiO_3$ film, we get $c = 4.095\,\text{Å}$and a thickness of $t = 22.5\,\text{nm}$.

In a superlattice, the $PbTiO_3/BaTiO_3$ bilayer creates a new unit cell. It also can be seen as a wavelength $\Lambda = n_P c_P + n_B c_B$ with $n_{P,B}$ the number of unit cells of $PbTiO_3$ and $SrTiO_3$ in each bilayer and $c_{P,B}$ their c-axes. A superlattice unit cell diffracts x-rays with the following Bragg condition:

$$2\Lambda \sin\theta_n = n\lambda \tag{5.4}$$

where θ_n is the angle of the nth peak. This equation allows to calculate Λ by

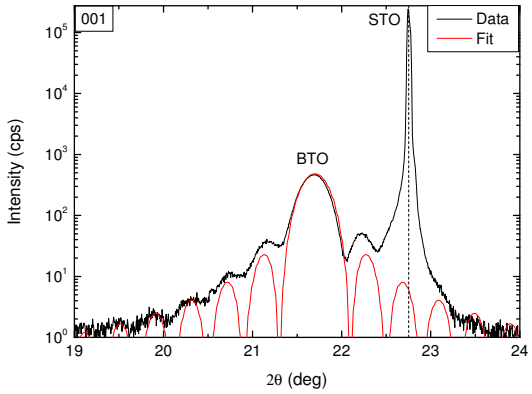

Figure 5.3: θ-2θ scan of an $BaTiO_3$ film (22.5 nm) on a $SrTiO_3$ substrate. The black line represents the data, and the red line is the fit.

using the angles θ_n and θ_{n-1} of the nth and the $(n-1)$th peak:

$$\Lambda = \frac{\lambda}{2} \frac{1}{\sin\theta_n - \sin\theta_{n-1}} \tag{5.5}$$

In a real sample, the number of unit cells per layer can deviate from the ideal integer. We can generalize the number of unit cells per layer by $n_P^{'} = n_P + \epsilon_P$ and $n_B^{'} = n_B + \epsilon_B$ with n_P and n_B integers and $0 < \epsilon_{P,B} < 1$. The real wavelength is then given by:

$$\Lambda = N\left(n_P^{'} c_P + n_B^{'} c_B\right) \tag{5.6}$$

where $N \in \mathbb{N}$ is the smallest integer which satisfies $N \cdot \epsilon_P \in \mathbb{N}$ and $N \cdot \epsilon_B \in \mathbb{N}$. The mean c-axis $\bar{c}$ of the superlattice is then given by

$$\bar{c} = \frac{n_P^{'} c_P + n_B^{'} c_B}{n_P^{'} + n_B^{'}}. \tag{5.7}$$

In Fig. 5.4 the θ-2θ diffractogram of an 6/5 $PbTiO_3/BaTiO_3$ superlattice shows the superlattice satellite peaks between the (000) and (002) reflections of the $SrTiO_3$ substrate. The peak, at slightly smaller angles than the (001) $SrTiO_3$ reflection is the nth peak (here 11). This nth peak corresponds to $\bar{c}$, allowing to determine its value. As long as the superlattice structure is constrained to the $SrTiO_3$ lattice parameter, we can use Bragg's law to calculate

$\bar{c}/a$:

$$\bar{c}/a = \frac{\lambda}{2\sin\theta_n}\frac{2\sin\theta_{substrate}}{\lambda} = \frac{\sin\theta_{substrate}}{\sin\theta_n} \tag{5.8}$$

In the following $\bar{c}/a$ will be called c/a for convenience. In this case $c/a = 1.059$ and can be used to calculate the mean c-axis value by using the known a-axis value of the $SrTiO_3$ substrate $a_S = 3.905$ Å, $\bar{c} = c/a \cdot a_S = 4.135$ Å. From the nth and $(n-1)$th peaks (here 11 and 10) we also can determine the pseudo wavelength Λ' by using Eq. 5.5 to $\Lambda' = 11.4\bar{c}$ which is close to $(6+5)\bar{c}$ the expected value from the growth parameter.

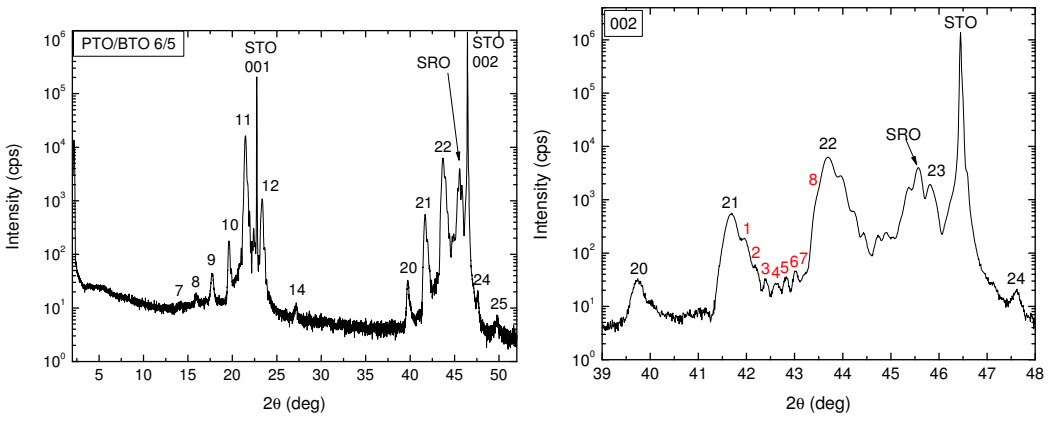

(a) (b)

Figure 5.4: (a) θ-2θ scan of an $PbTiO_3/BaTiO_3$ 6/5 superlattice with 10 bilayers. Form the 11^{th} peak $\bar{c}$ can be determined. (b) The 8 smaller peaks between two superlattice satellite peaks are due to the 10 bilayers of the superlattice.

Due to the number m of bilayers in the film, we also see the $m-2$ size effect oscillations between the satellite peaks. In this superlattice, we have 10 bilayers which generates 8 peaks in between the main superlattice peaks (see Fig. 5.4(b)).

5.1.3 Reciprocal space maps

The reciprocal space (RS) around peaks with an in-plane component can mapped out by varying ω and performing ω - 2θ scans. The χ and ϕ angle are fixed and define the region in the RS which is measured. However, with our Bruker Discover D8 we can perform linear q scans in the RS which allows us to define exactly the rectangle in RS which is of interest. We looked at regions in the RS around the $(\bar{1}\bar{1}3)$ reflection of your $SrTiO_3$ substrates, as

shown in Fig. 5.5. The x-axis corresponds to $(hk3)$ with $h = k$, and gives information on the in-plane lattice parameters a and b. The y-axis corresponds to $(11l)$ and gives information on the out-of-plane lattice parameter c. From the position of the peak we can determine if the film was grown coherently on the substrate or if it is partially or fully relaxed. If the film peak is vertically aligned with the substrate peak we have a coherent growth (see Fig. 5.5). If the peaks are not aligned, we have a partially or fully relaxed film.

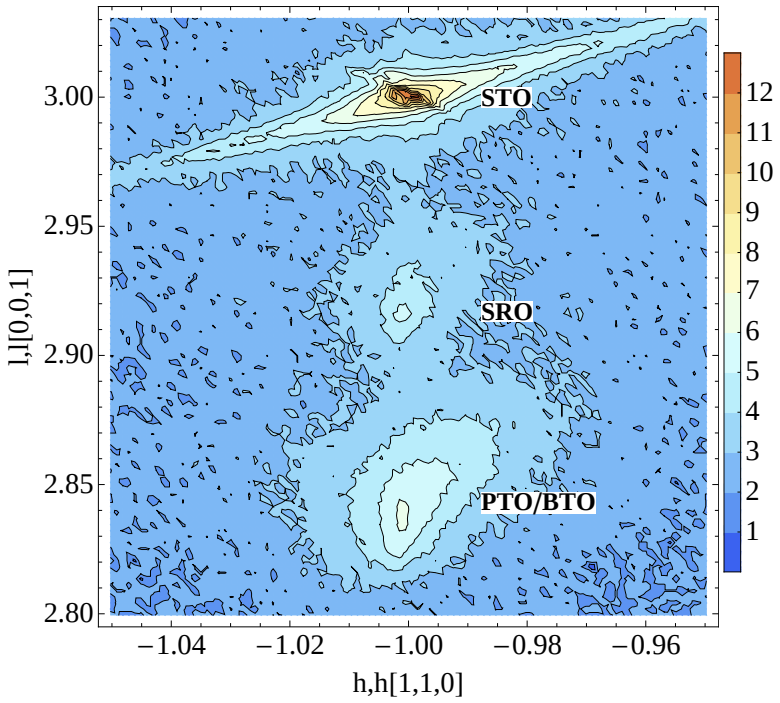

Figure 5.5: Reciprocal space map of an $PbTiO_3/BaTiO_3$ superlattice around the $(\bar{1}\bar{1}3)$ peak in hkl units. The superlattice peak and the $SrRuO_3$ electrode peak showing the coherent growth on the substrate.

Fig. 5.5 shows the reciprocal space map of an 6/5 $PbTiO_3/BaTiO_3$ superlattice. The $SrRuO_3$ electrode peak as well as the $PbTiO_3/BaTiO_3$ superlattice peak can be seen and are coherent with the $SrTiO_3$ substrate.

5.2 X-ray low-angle reflectometry

The x-ray low-angle reflection measurement can be used to determine the thickness of a film. Fig. 5.6 shows a low-angle reflection curve of a $SrRuO_3$ film. The oscillations are due to the finite size of the film and can be used to determine the thickness t of the film. If we assume the dynamically formulation of x-ray reflection and a sufficiently small incidence angle α_i, we get the following approximation [15]:

$$\alpha_{i\,m}^2 - \alpha_c^2 = m^2 \left(\frac{\lambda}{2t}\right)^2, \tag{5.9}$$

where α_c is the critical angle of total external reflection of the layer, m is an integer and λ is the wavelength of the x-rays. With the slope s in a linear fit of $\alpha_{i\,m}^2$ over m^2 the thickness t of the thin film can be determined by:

$$t = \frac{\lambda}{2\sqrt{s}}. \tag{5.10}$$

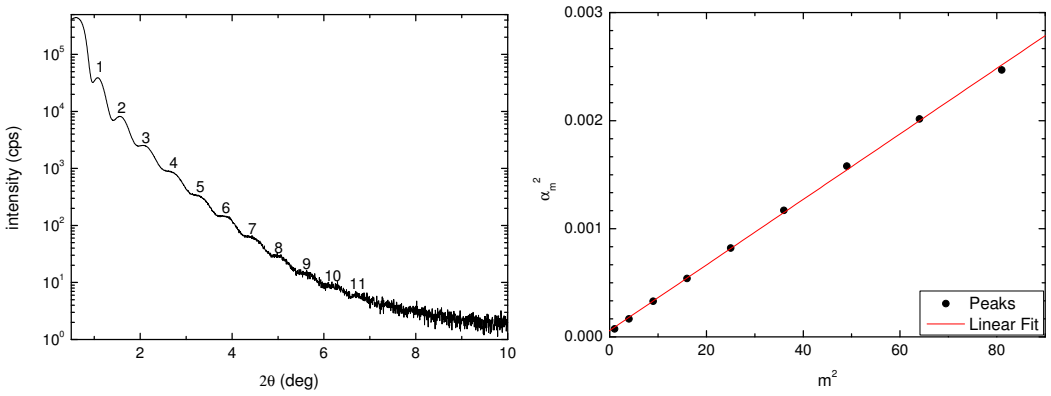

(a) (b)

Figure 5.6: (a) Low-angle reflection scan. (b) α_m^2 - m^2 plot with linear fit.

The thickness for the $SrRuO_3$ film (Fig. 5.6) can be determined with Eq. 5.10 to $t = 14\,\text{nm}$. The reader is referred to [15] for more details on thin film and multilayer reflection and diffraction.

5.3 Atomic force microscopy

5.3.1 Topographic measurements

To grow high quality superlattices, it is essential to have an atomical flat surfaces. In order to get information of the surface quality, we performed atomic force microscope (AFM) topographic measurements on our Asylum Research MFP-3D-SA. The sample roughnesses were typically in the range from 1 Åto 6 Å. Fig. 5.7(a) shows the topography of an $5 \times 5\,\mu m^2$ area of a relaxed $BaTiO_3$ thin film (64.5 nm) grown at 650 °C with a surface roughness of 1.7 Å. The picture also shows the steps of the substrate miscut, which form as a result of a buffered HF treatment that produces a surface that has only TiO_2 termination.

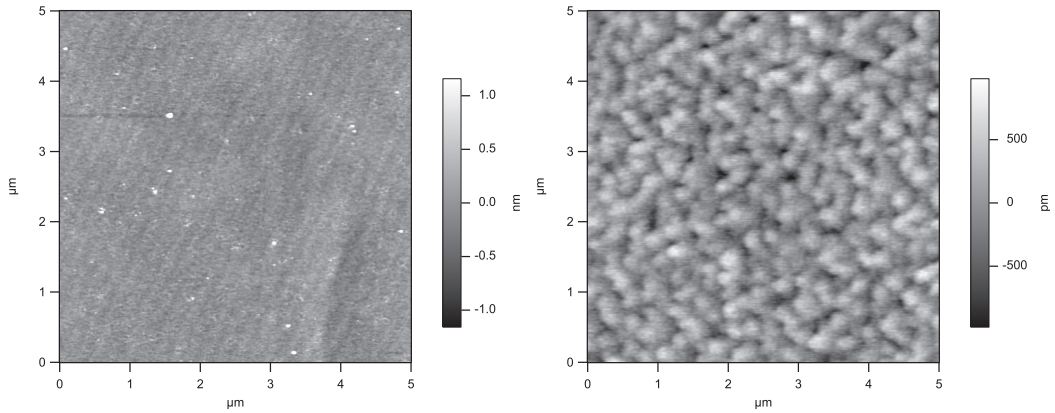

(a) $BaTiO_3$ (b) $PbTiO_3$

Figure 5.7: (a) Topography of a relaxed $BaTiO_3$ thin film (64.5 nm) with a surface roughness of 1.7 Å. (b) Topography of a $PbTiO_3$ film (14 nm) on a $SrRuO_3$ electorde (24 nm) with a roughness of 2.4 Å.

Fig. 5.7(b) shows the topography of a $5 \times 5\,\mu m^2$ area of a $PbTiO_3$ thin film (14 nm) with a $SrRuO_3$ bottom electrode. The roughness is 2.4 Åbut no steps are visible.

5.3.2 Piezorsponse force microscopy

To test the ferroelectricity and the piezoelectric effect of our samples, we used the piezoresponse mode of our AFM. In order to write and read domain structures, we wire-bonded the $SrRuO_3$ bottom electrode of our thin films and

superlattices. To write domains, we applied a sufficiently high voltage [1] to the AFM tip and wrote a pattern on our samples in contact mode. The polarization was then read in dual-frequency resonance-tracking mode [16].

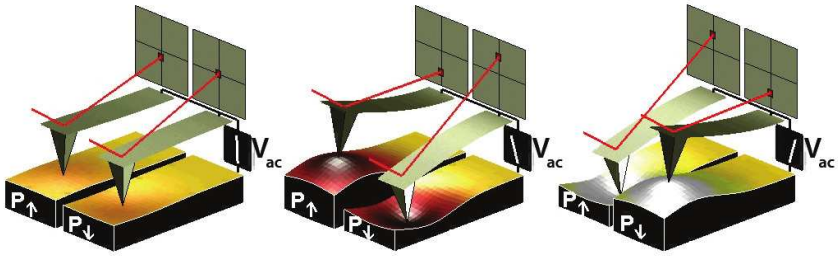

Figure 5.8: Dependence of the sample strain on the voltage sign. When the domains have a vertical polarization that is pointed downwards and a positive voltage is applied to the tip, the sample will locally expand. If the polarization is pointed up, the sample will locally contract. The phase of the measured response is thus proportional to the direction of the domain polarization.

To read the piezoelectric domains a voltage is applied to the sample surface with a conductive tip of the AFM in contact mode. In responds to the direction of the applied bias and the direction of the polarization in the domain, the sample is locally contracted or expanded (see Fig. 5.8).

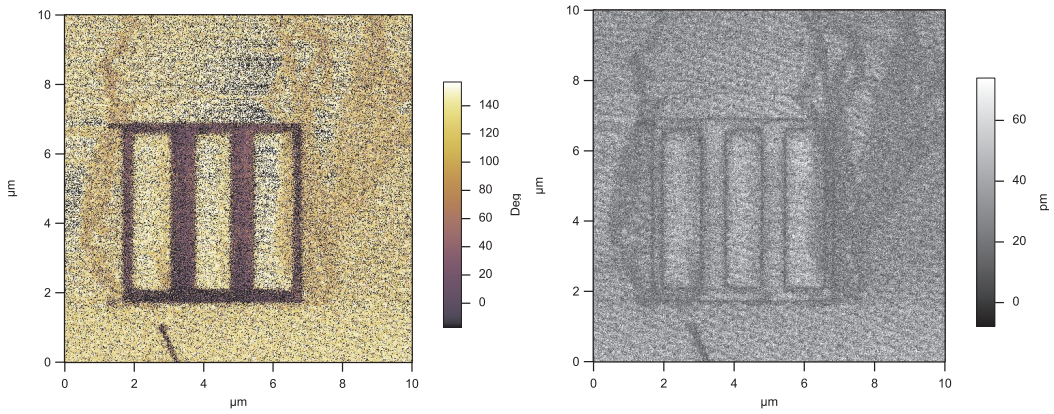

(a) Phase (b) Amplitude

Figure 5.9: PFM phase (a) and amplitude (b) image of a written domain structure on a $BaTiO_3$ thin film. The color yellow and purple indicate the two opposite polarization directions (180°) of the domains in the phase image. The darker straight lines represent the domain walls in the amplitude image.

[1] Higher than the coercive field, typically around 11 V

For all our samples we have not found any natural domain structure that is resolvable within the resolution of the instrument. To write domains we usually polarized an area of $10 \times 10\,\mu\mathrm{m}^2$ in one direction and wrote then a pattern in the opposite direction. Fig. 5.9(a) shows the phase picture of a $10 \times 10\,\mu\mathrm{m}^2$ area. The colors yellow and purple indicate the two opposite polarization directions. The domain walls can be seen in the amplitude in Fig. 5.9(b).

In addition to these images which confirm the ferroelectric nature of the samples, PFM can also be used to quantitatively measure the piezoresponse of a sample. However, doing this accurately is complicated and requires either modelling of the resonant properties and field distribution of the tip and is greatly aided by top electrodes. We are in the process of optimizing our techniques and will soon begin photolithographic electrode fabrication, but as these efforts are at an early stage they will not be presented here.

Chapter 6

Growth conditions for $BaTiO_3$

One main part of the work was to find good growth conditions for $BaTiO_3$ thin films, something that was not required for $PbTiO_3$ and $SrRuO_3$ where the growth conditions were adopted from previous work [5]. In this chapter, I describe where we started and how we found good growth settings.

6.1 $BaTiO_3$ thin films

The reported growth conditions for $BaTiO_3$ vary over a broad pressure range from 0.015 Torr [17] to 1.95 Torr [18] for different deposition techniques. We started to grow films with the lowest possible pressure (40 mTorr) at which the rf sputter guns produced a reliable plasma. This lower pressure limit was set by the gun power since a much larger power ($\sim 50-60$ W) would be necessary to start the plasma which is undesired because it results in a much higher growth rate. At a pressure of 60 mTorr we were growing a series of samples for different growth temperatures from 550 °C to 700 °C (Fig. 6.1(a)). The Ar/O ratio was 2/1. All films have a thickness of 64.5 nm. In Fig. 6.1(b), the in-plane lattice parameter $a$and the out-of-plane lattice parameter c are shown. The highest c/a ratio is achieved for a growth temperature of 650 °C which was used for the later $BaTiO_3$ thin films. As can be seen in Fig. 6.1(b), the $BaTiO_3$ films are relaxed, which is most likely due to the thickness of the films and non-optimal growth conditions. We notice that a is for all samples higher than the tetragonal bulk value of $BaTiO_3$ ($a = 3.99$ Å). For a thinner film (22.5 nm) (blue star) grown at a lower pressure ($p = 40$ mTorr) the relaxation was found to be slightly smaller.

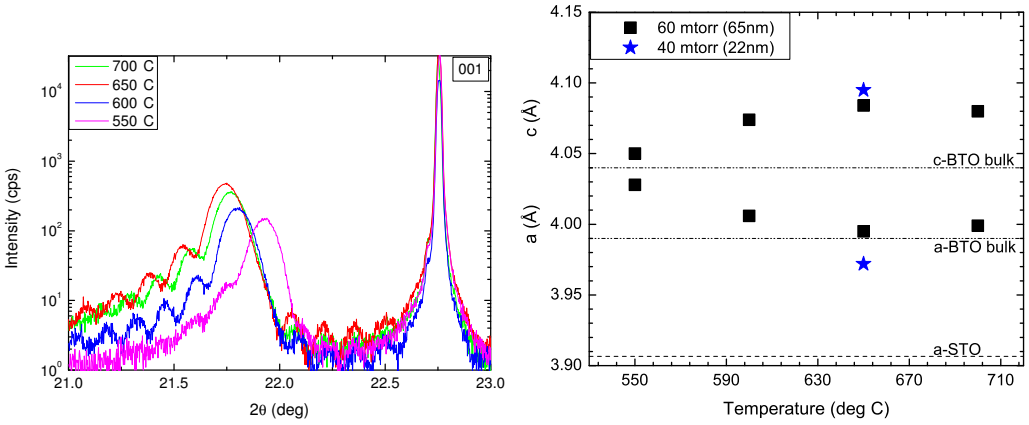

(a) (b)

Figure 6.1: (a)X-ray θ-2θ scans of a series of $BaTiO_3$ thin films (64.5 nm) grown at different temperatures. (b) Dependence of the a and c lattice parameter on the temperature (black squares). It also shows the lattice parameter for a thinner $BaTiO_3$ film (22 nm), grown at a lower pressure (40 mTorr). The dashed lines indicate the bulk $BaTiO_3$ and $SrTiO_3$ lattice parameter.

Fig. 6.2 shows the RSM around the $(\bar{1}\bar{1}3)$ substrate peak. The $BaTiO_3$ film is clearly relaxed. This was found for all $BaTiO_3$ films at different growth conditions without a $SrRuO_3$ bottom electrode.

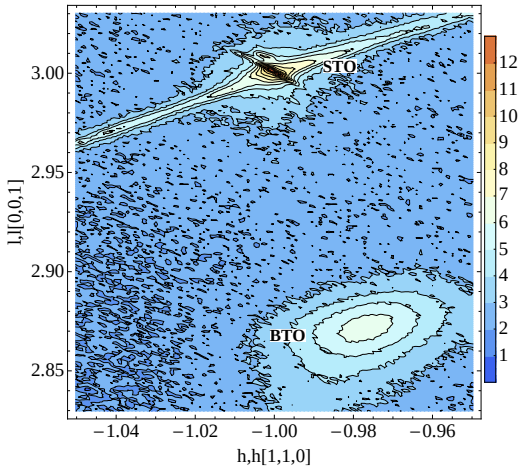

Figure 6.2: RSM around the $(\bar{1}\bar{1}3)$ substrate peak of the relaxed $BaTiO_3$ film (64.5 nm) grown at 650 °C.

From this result we can presume that the critical thickness of totally strained $BaTiO_3$ on $SrTiO_3$ substrates is extreme small. This is consistent with results reported by M. Kawai et al. [19]. They found an increase of the critical thicknesses with an increase of the growth rate. Samples grown with a same growth rate as ours (0.01 nm/s) were all found to be relaxed. Strained films were only found with four times higher growth rates.

6.2 Influences of $SrRuO_3$ as bottom electrode

In order to perform PFM measurements, it is necessary to have a good bottom electrode. We chose $SrRuO_3$ because of the reasons mentioned in 3.2. The change in the lattice parameter for the $BaTiO_3$ film on top of a $SrRuO_3$ electrode were found to be huge compared to the change in absence of a bottom electrode. Fig. 6.3(a) shows the θ-2θ scans of one samples with and one sample without an electrode ($t_{electrode} = 20\,\text{nm}$). The c lattice parameter of the $BaTiO_3$ films are 4.095 Åand 4.205 Årespectively. The thickness of the $BaTiO_3$ film is for both samples $t = 22.5\,\text{nm}$. The in-plane lattice parameter a was determined from a RSM. Fig. 6.4 shows the RSM for the only slightly relaxed sample ($a = 3.914\,\text{Å}$) with an electrode. The film without an electrode was found to be relaxed ($a = 3.972\,\text{Å}$). The c/a ratio are 1.078 and 1.031 for the

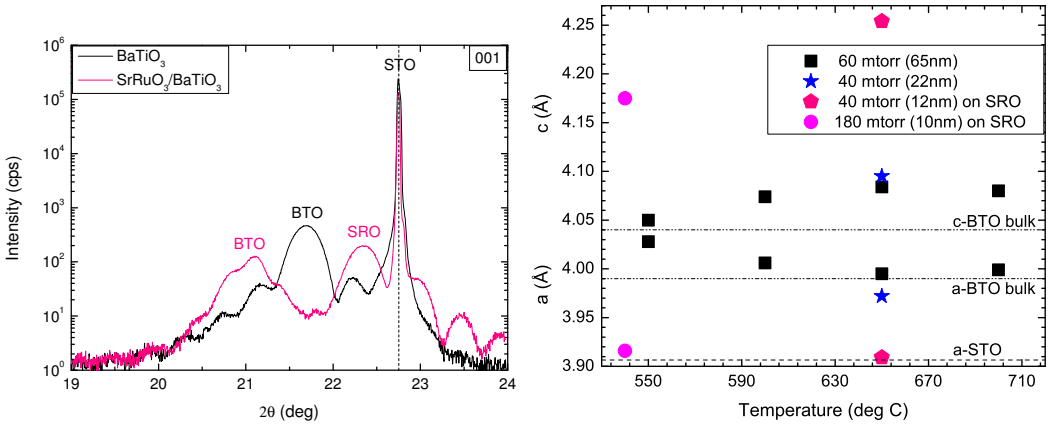

(a) (b)

Figure 6.3: (a) X-ray θ-2θ scans for a $BaTiO_3$ thin film and one on top of a $SrRuO_3$ bottom electrode. A huge change in the c lattice parameter can be seen. (b) The coherent growth can be seen from the lattice parameter for the $BaTiO_3$ on $SrRuO_3$ (red). The purple data points show the almost coherent growth for $BaTiO_3$ on $SrRuO_3$ at the $PbTiO_3$ growth conditions.

film with and without an electrode. The thickness of the $BaTiO_3$ layer was found to have an influence on both lattice parameter. A $BaTiO_3$ film with thickness $t = 11.5\,\text{nm}$ had an c/a ratio of 1.088 ($a = 3.909\,\text{Å}$, $c = 4.254\,\text{Å}$). The lattice parameter of our $SrRuO_3/BaTiO_3$ films are consistent with reported ones in [20]. For $BaTiO_3$ films grown on (110) $DyScO_3$ an effect of an intermediate $SrRuO_3$ electrode on the c lattice parameter was found but c changed only very little from $c_{w/o} = 4.0953\,\text{Å}$to $c_w = 4.0989\,\text{Å}$[3]. This change was found even though films were coherent with the substrate in-plane lattice parameter. One reason the effect may be smaller is due to the smaller lattice mismatch between $BaTiO_3$ and $DyScO_3$ ($\sim 1.7\,\%$) compared to the one with $SrTiO_3$ ($\sim 2.2\,\%$).

A possible reason for the large change in coherence and c might be in the screening of the depolarization field by the metallic $SrRuO_3$ electrode.

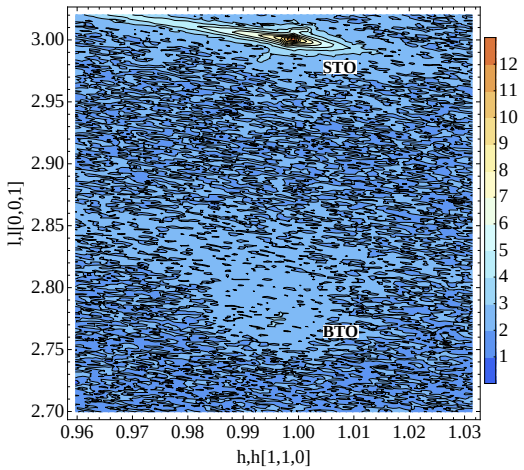

Figure 6.4: RSM around the $(\bar{1}\bar{1}3)$ substrate peak of the almost coherent $BaTiO_3$ film on $SrRuO_3$ grown at 650 °C, 40 mTorr.

6.3 $PbTiO_3$ films

Two $PbTiO_3$ films (15 nm) with and without a $SrRuO_3$ electrode were found to be coherent. The out-of-plane lattice parameter c changed from $c = 4.120\,\text{Å}$without electrode to $c_{el} = 4.110\,\text{Å}$. The c/a ratios are 1.055 and 1.052 respectively. It can be seen that there is almost no influence of a $SrRuO_3$ electrode on the $PbTiO_3$ films. Our results are consistent with work done by researchers at Argonne National Lab for $PbTiO_3/SrTiO_3$ and $PbTiO_3/SrRuO_3/SrTiO_3$

systems where the effect of the $SrRuO_3$ electrode layer is vanishing for $PbTiO_3$ films thicknesses of 15 nm. For thinner films a difference in the transition temperature and thus a difference in c are expected [21].

6.4 $BaTiO_3$ grown at $PbTiO_3$ conditions

Our growth chamber is fully computer controlled, which means that the growth parameter for each material can be controlled during the growth on its own. We tried to grow $PbTiO_3/BaTiO_3$ superlattices while changing the growth condition between each layer of $PbTiO_3$ and $BaTiO_3$ to the optimal ones found for each individual material. These samples did not show any superlattice x-ray diffraction peaks. Another unsuccessful attempt was to keep the growth temperature constant at $PbTiO_3$ temperature (540 °C) and only changed the pressure and Ar/O ratio.

For $PbTiO_3/SrTiO_3$ superlattices grown in rf off-axis sputtering technique the best results were archived by keeping the growth conditions equal for both materials at the low temperature conditions for $PbTiO_3$ [5].

A $BaTiO_3$ film (10 nm) grown at the $PbTiO_3$ growth conditions was found to be only slightly relaxed with $a = 3.916$ Åand $c = 4.180$ Å(see Fig. 6.3(b), purple circle). The tetragonalitly is $c/a = 1.068$.

Chapter 7

$PbTiO_3/BaTiO_3$ superlattices

7.1 Theoretical predictions

A density functional theory (DFT) calculation by V.R. Cooper and K.M. Rabe predicts an enhancement of the piezoelectric response for $PbTiO_3/BaTiO_3$ superlattices [22]. Fig. 7.1 shows the dependency of the polarization and c/a ratio on the $PbTiO_3$ concentration in the superlattice. The polarization along the z-axis stays almost constant up to 50 % $PbTiO_3$ in the superlattice, and also the c/a ratio shows an unusual behavior in the range of 50 % to 100 % $PbTiO_3$ where it has a minimum which is below the c/a ratio for pure $PbTiO_3$. From a simple linear interpolation we would expect a straight line between the pure $BaTiO_3$ and pure $PbTiO_3$ points.

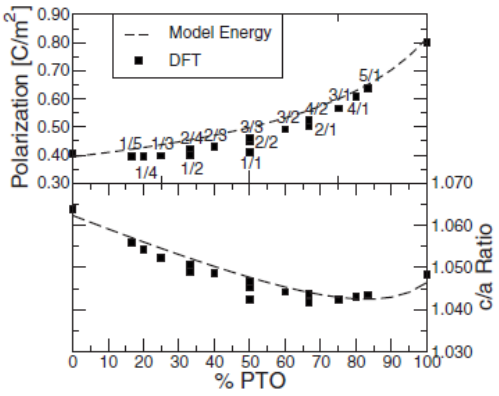

Figure 7.1: Dependence of the polarization (top) and c/a ratio (bottom) on the $PbTiO_3$ concentration and the superlattice periodicity. Black squares are the DFT calculations, and the dashed lines represent the values of a superlattice model. Figure from [22].

To explain the behavior of the superlattices, the authors used an expression for the effective enthalpy which is explained in detail in [22]. Fig. 7.2 (left) shows the evolution of the effective enthalpy for the pure $BaTiO_3$ (dashed), the pure $PbTiO_3$ (dashed-dotted), and four compositions of $PbTiO_3/BaTiO_3$ superlattices at 20 % $PbTiO_3$ intervals. The minimum in the energy well for pure $BaTiO_3$ is at a polarization less than half of pure $PbTiO_3$. Furthermore, the energy well for $BaTiO_3$ has a sharp increase above its minimum at $0.39\,\mathrm{C/m^2}$ while the dependence for pure $PbTiO_3$ is much gentler. At this P the $BaTiO_3$ layers are saturated and need a larger electric field to be further polarized. In a superlattice a higher percentage of $PbTiO_3$ is necessary to increase the macroscopic polarization but even up to $PbTiO_3$ concentration of 80 % the enthalpy well resembles the $BaTiO_3$ well. This behavior is the reason for the suppressed polarization up to 50 % $PbTiO_3$. Fig. 7.2 on the right shows the coupling between the c lattice parameter and the polarization. The open circles represent c for the minima of the energy wells on the left. For a certain concentration of $PbTiO_3$ in the superlattice is the c lattice parameter below the strained $PbTiO_3$ value (dotted line). This drastic reduction of c is the reason for the minimum in the c/a ratio at about 75 % $PbTiO_3$ in the superlattice. This effect is only overcome at very high concentrations of $PbTiO_3$ when the polarization of the $PbTiO_3$ layers can counteract the $BaTiO_3$ energy well constraints.

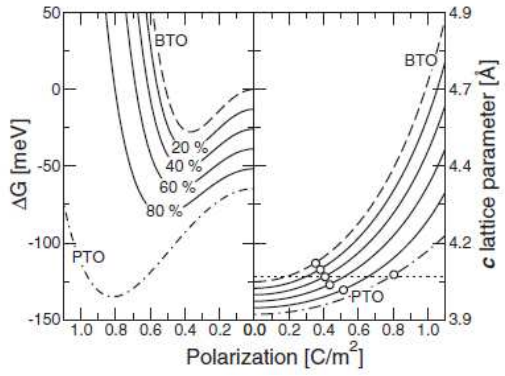

Figure 7.2: Dependence of the effective enthalpy (left) and the c lattice parameter (right) on the polarization for different compositions of $PbTiO_3/BaTiO_3$ superlattices. Dashed lines represent pure $BaTiO_3$, dashed-dotted lines are for pure $PbTiO_3$, and the solid lines are for superlattice compositions. Open circles indicate the c lattice parameter for each composition at the predicted polarization. The dotted line represents c for the epitaxially strained $PbTiO_3$. Zero energy is set to the epitaxially strained bulk $BaTiO_3$ value. Figure from [22]

The much steeper slope in the P-c dependence in $BaTiO_3$ means that the c lattice parameter is increasing more in $BaTiO_3$ than in $PbTiO_3$ for increasing P. This stronger polarization-strain coupling in the $BaTiO_3$ layers and the concentration of $PbTiO_3$ which poles these layers creates the peak in d_{33} at $\sim 75\,\%$ $PbTiO_3$ concentration (see Fig. 7.3).

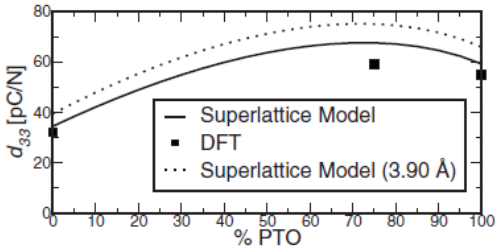

Figure 7.3: Dependence of d_{33} on the $PbTiO_3$ concentration. Black squares are computed from DFT, the solid line represents the results from the superlattice model for $SrTiO_3$ in-plane lattice values (3.863 Å), and the dotted line are the results for a slightly higher in-plane lattice constant (3.90 Å). We notice, the lattice parameter calculated by DFT are typically smaller than experimental values. Figure from [22]

7.2 Experiment

All our superlattice were grown on (001) $SrTiO_3$ substrates with a 20 nm thick $SrRuO_3$ electrode in between. The best superlattices were grown when the growth conditions for both materials, $PbTiO_3$ and $BaTiO_3$, were equal (see Tab. 4.1). The optimal temperature was found to be 550 °C. The number of bilayers in the structure were chosen to have a constant thickness of the superlattice of $t \sim 50$ nm to get comparable results from sample to sample in electrical measurements. For samples with a $PbTiO_3$ concentration below 50 % relaxation of the in-plane lattice parameter was found. Therefore, we grew these samples with a total thickness of only $t = 10$ nm to minimize the relaxation.

7.2.1 Structural characterization

X-ray diffraction was used to check the crystalline quality and to determine the mean c-axis $\bar{c}$ and the pseudo wavelength Λ'. Fig. 7.4 shows the θ-2θ scans of three samples, illustrating the change of the satellite peak position with Λ'. The expected number of unit cells per bilayer, $\bar{c}$, and Λ' are given

in each graph. The expected number of unit cells per bilayer matches the measured ones fairly good. The size effect due to the finite number of bilayers can be seen between the satellite peaks of all samples, very clear on top of the $SrRuO_3$ peak. The number of bilayers are 10, 15, and 12 for the 6/5, 4/3, and 7/3 sample.

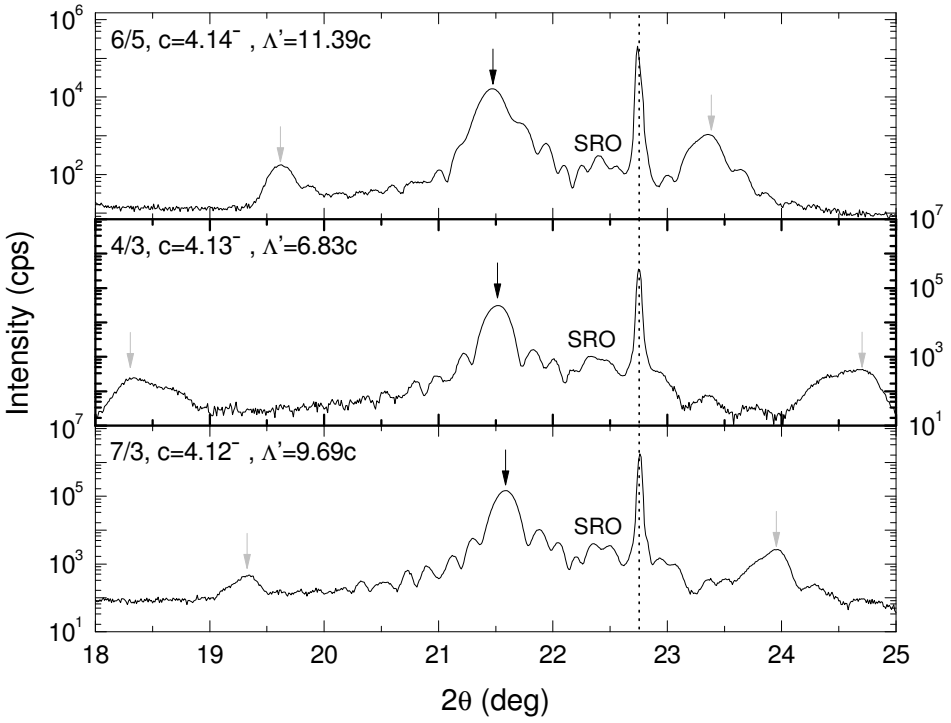

Figure 7.4: θ-2θ scans of 3 different superlattices. The black arrow indicate the reflection peak corresponding to c, the grey arrows the satellite peaks. The dotted line corresponds to the (001) reflection of the $SrTiO_3$ substrate. The $SrRuO_3$ electrode reflection peak is indicated by SRO.

7.2.2 Tetragonality

For all superlattices we performed RSM measurements to verify the coherence of the in-plane lattice parameters. Fig. 7.5 shows the dependence of c/a on the $PbTiO_3$ concentration for the experimental values (red) and the theoretical prediction (black). All superlattice samples have a total thickness of 50 nm except of the one with 40 % $PbTiO_3$ concentration which is only 10 nm thick. The pure $BaTiO_3$ and the pure $PbTiO_3$ film have a thickness of 10 nm and 15 nm respectively. The two samples marked with an asterisk were found to

be slightly relaxed due to the non-optimal growth conditions for $BaTiO_3$. All errors were estimated from the peak positions. The error in the $PbTiO_3$ volume fraction is smaller than the squares. Unlike the DFT calculations which predict a minimum around 75 %, our experimental data show a linear dependence of c/a on the $PbTiO_3$ concentration (dotted line).

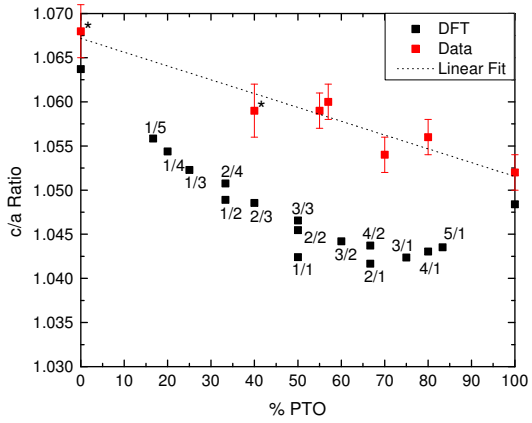

Figure 7.5: c/a ratio vs. $PbTiO_3$ concentration. The black squares represent the DFT calculations, the red squares the experimental data, the dotted line is the best linear fit to the data.

7.2.3 Discussion

There is an importance difference between the DFT calculations, which are at zero temperature, and our measurements which were done at room temperature. In the simplest form of the Landau theory where only the quadratic coefficient has temperature dependence this should not cause a difference in the evolution of the polarization across the superlattice series. However, $BaTiO_3$ turns out to be a special case. J. Iniguez et al. found with first principle calculations for the Landau-Devonshire free energy of $BaTiO_3$ a strong temperature dependence of the fourth-order coefficients [23]. The free energy potential can be written as:

$$F = F_0 + \frac{1}{2}a(P_x^2 + P_y^2 + P_z^2) + uP^4 + v(P_x^4 + P_y^4 + P_z^4) + \text{ (higher order terms)}$$

where F_0 is the free energy of the reference cubic phase and a, u and v are temperature dependent coefficients. Fig. 7.6 shows the free energy coefficients for non strained $BaTiO_3$, the fourth-order parameter u and v show a strong

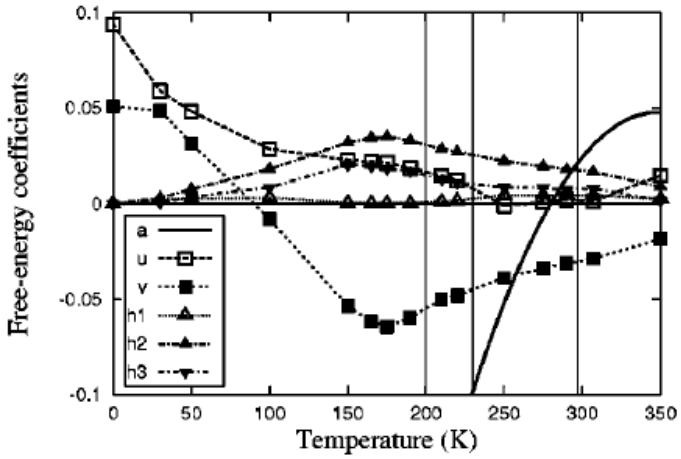

Figure 7.6: Free energy coefficient of $BaTiO_3$ optained from Monte Carlo simulations. Figure from [23].

temperature dependence between zero temperature and room temperature and v even changes signs, this means bulk $BaTiO_3$ has a first order transition between the paraelectric and ferroelectric phase.

Although the superlattice $BaTiO_3$ is strained and not bulk like as in the calculations, a temperature dependence of the coefficients is still expected. This was shown for strained films in [24]. Since our crystal system is highly compressively strained in-plane and therefore tetragonal, the polarization is constrained in the out-of-plane direction z and leads to $P_x = P_y = 0$. This simplifies the fourth-order to $(u+v)P_z^4$ + (strain dependent contribution). In [24] it was shown that strained $BaTiO_3$ has a second-order phase transition between paraelectric and ferroelectric phase for negative misfit strains. This means the fourth-order parameter is positive but smaller than for zero temperature. Therefore we might expect a softer slope of the free energy potential well, lowering the suppression of the polarization due to the $BaTiO_3$ layers in the superlattice. This may then explain our observed linear or almost linear dependence of the polarization and c/a ratio on the $PbTiO_3$ concentration.

Chapter 8

Conclusion and perspective

We succesfully built a new rf off-axis sputtering chamber with a novel shutter design and started to grow nice atomically flat ferroelectric thin films and superlattices. We were growing $BaTiO_3$ thin films at various conditions with and without $SrRuO_3$ electrodes and performed x-ray diffraction and low-angle x-ray reflection measurement to determine the crystalline quality and the thickness of our samples. We found the temperature of 650 °C to give the most strained $BaTiO_3$ films in our chamber. Furthermore, we found a surprising effect of the bottom electrode on the strain of the $BaTiO_3$ film and believe this effect is due to the screening of the depolarization field by the metallic electrode. In future work, we will try to grow $BaTiO_3$ thin films which are more perfectly constrained to the (001) $SrTiO_3$ substrate by the use of a higher growth rate. It was reported for $BaTiO_3/SrTiO_3$ as well as $BaTiO_3/SrRuO_3/SrTiO_3$ systems that an increase in the growth rate follows in an increase in the critical thickness of constrained thin films [25]. We also checked the surface roughness of the samples with our AFM and measured very low roughnesses of < 1 Å to 6 Å. We could also measure a step-terrace structure on the surface.

The growth of $PbTiO_3$ thin films was straight forward and did not show any significant effects on the $SrRuO_3$ electrode. This is found to be consistent with [21]. In our attempts to grow $PbTiO_3/BaTiO_3$ superlattices we achieved the best results when both materials were grown at the $PbTiO_3$ growth conditions. We were growing coherent $PbTiO_3/BaTiO_3$ superlattices for $PbTiO_3$ concentrations over 50 %. Superlattices with the same thickness and with an concentration under 50 % $PbTiO_3$ were found to be partially or fully relaxed, depending on the thickness. However, very thin but still slightly relaxed samples were used to compare the experimental data with the theoretical predictions. We performed x-ray diffraction measurements to determine the crystalline quality and the c/a ration as function of the $PbTiO_3$ concentration. The non-linear dependence of c/a with an minimum around 75 % $PbTiO_3$ of

the DFT calculations was not found in our data which are indicating a more linear behavior. This difference is based on the temperature dependence of the fourth-order free energy coefficients of $BaTiO_3$ [23],[24] since the theoretical calculations assume zero temperature but our measurements were done at room temperature. The vanishing fourth-order coefficient softens the steep zero temperature free energy well for $BaTiO_3$ at room temperature. This leads to the observed linear dependence of c/a on the $PbTiO_3$ concentration.

In the future it is planned to optimize the quality of $BaTiO_3$ thin films by increasing the growth rate. This should allow us to fabricate high quality $PbTiO_3/BaTiO_3$ superlattices over the whole range from 0 % to 100 % $PbTiO_3$ concentration. Furthermore, low temperature x-ray measurements could be performed to compare the experimental data better with the DFT predictions. Finally, samples with $SrRuO_3$ top electrodes will be grown to perform electrical measurements (polarization and dielectric constant) and furthermore to measure quantitatively the piezoelectric coefficient d_{33} so that we can directly test the theoretical predictions of an enhancement of the piezoresponse in $PbTiO_3/BaTiO_3$ superlattices.

Bibliography

[1] J. Valasek. Piezo-electric and allied phenomena in Rochelle salt. *Physical review*, 17:475–481, 1921.

[2] B.M. Wul and I.M. Goldman. Dielectric constants of titanates of metals of the second group. In *Dokl. Akad. Nauk SSSR*, volume 46, pages 154–57, 1945.

[3] K.J. Choi, M. Biegalski, Y.L. Li, A. Sharan, J. Schubert, R. Uecker, P. Reiche, Y.B. Chen, X.Q. Pan, V. Gopalan, et al. Enhancement of ferroelectricity in strained $BaTiO_3$ thin films. *Science*, 306:1005–1009, 2004.

[4] J.B. Neaton and K.M. Rabe. Theory of polarization enhancement in epitaxial $BaTiO_3/SrTiO_3$ superlattices. *Applied Physics Letters*, 82:1586, 2003.

[5] M. Dawber and C. Lichtensteiger and M. Cantoni and M. Veithen and P. Ghosez and K. Johnston and K.M. Rabe and J.-M. Triscone. Unusual Behavior of the Ferroelectric Polarization in $PbTiO_3/SrTiO_3$ Superlattices. *Phys. Rev. Lett.*, 95:177601, 2005.

[6] E. Bousquet, M. Dawber, N. Stucki, C. Lichtensteiger, P. Hermet, S. Gariglio, J.M. Triscone, and P. Ghosez. Improper ferroelectricity in perovskite oxide artificial superlattices. *Nature*, 452:732–736, 2008.

[7] R.E. Cohen. Origin of ferroelectricity in perovskite oxides. *Nature*, 358: 136–138, 1992.

[8] M.E. Lines and A.M. Glass. *Principles and applications of ferroelectrics and related materials*. Oxford, 1977.

[9] K.M. Rabe, C.H. Ahn, and J.-M. Triscone. *Physics of Ferroelectrics: A Modern Perspective*. Springer, 2007.

[10] H.F. Kay and P. Vousden. Symmetry changes in barium titanate at lox temperatures and their relation to its ferroelectric properties. *Philosophical Magazine*, 40:1019–1040, 1949.

[11] B. Jaffe, W. R. Cook Jr., and H. Jaffe. *Piezoelectric ceramics*. Number 4. 1972.

[12] C.B. Eom, R.J. Cava, R.M. Fleming, J.M. Phillips, R.B. Vandover, J.H. Marshall, J.W.P. Hsu, J.J. Krajewski, and W.F. Peck. Single-crystal epitaxial thin films of the isotropic metallic oxides $Sr_{1-x}Ca_xRuO_3$ ($0 \leq x \leq 1$). *Science*, 258:1766–1769, 1992.

[13] Nicolas Stucki. *Artificial Ferroelectric Materials*. PhD thesis, University of Geneva, 2008.

[14] J.H. Haeni, P. Irvin, W. Chang, R. Uecker, P. Reiche, Y.L. Li, S. Choudhury, W. Tian, M.E. Hawley, B. Craigo, et al. Room-temperature ferroelectricity in strained $SrTiO_3$. *Nature*, 430:758–761, 2004.

[15] V. Holy, U. Pietsch, and T. Baumbach. *High-Resolution X-Ray Scattering from Thin Films and Multilayers*. Springer Tracts in Modern Physics. Springer, 1999.

[16] B.J. Rodriguez, C. Callahan, S.V. Kalinin, and R. Proksch. Dual-frequency resonance-tracking atomic force microscopy. *Nanotechnology*, 18:475504, 2007.

[17] Hsi-Nao Tsai, Yuan-Chang Liang, and Hsin-Yi Lee. Characteristics of sputter-deposited $BaTiO_3/SrTiO_3$ artificial superlattice films on an $LaNiO_3$-coated $SrTiO_3$ substrate. *Journal of Crystal Growth*, 284:65–72, 2005.

[18] A. Petraru, H. Kohlstedt, U. Poppe, R. Waser, A. Solbach, U. Klemradt, J. Schubert, W. Zander, and N. A. Pertsev. Wedgelike ultrathin epitaxial $BaTiO_3$ films for studies of scaling effects in ferroelectrics. *Applied Physics Letters*, 93:072902, 2008.

[19] M. Kawai, D. Kan, S. Isojima, H. Kurata, S. Isoda, Y. Shimakawa, S. Kimura, and O. Sakata. Critical thickness control by deposition rate for epitaxial $BaTiO_3$ thin films grown on $SrTiO_3(001)$. *Journal of Applied Physics*, 102:114311, 2007.

[20] Y.S. Kim, D.H. Kim, J.D. Kim, Y.J. Chang, T.W. Noh, J.H. Kong, K. Char, Y.D. Park, S.D. Bu, J.-G. Yoon, and J.-S. Chung. Critical

thickness of ultrathin ferroelectric $BaTiO_3$ films. *Applied Physics Letters*, 86:102907, 2005.

[21] D.D. Fong, A.M. Kolpak, J.A. Eastman, S.K. Streiffer, P.H. Fuoss, G.B. Stephenson, C. Thompson, D.M. Kim, K.J. Choi, C.B. Eom, I. Grinberg, and A.M. Rappe. Stabilization of Monodomain Polarization in Ultrathin $PbTiO_3$ Films. *Physical Review Letters*, 96:127601, 2006.

[22] V.R. Cooper and K.M. Rabe. Enhancing piezoelectricity through polarization-strain coupling in ferroelectric superlattices. *Physical Review B*, 79:180101, 2009.

[23] J. Íñiguez and S. Ivantchev and J.M. Perez-Mato and A. García. Devonshire-Landau free energy of $BaTiO_3$ from first principles. *Phys. Rev. B*, 63:144103, 2001.

[24] N.A. Pertsev and A.G. Zembilgotov and A.K. Tagantsev. Effect of Mechanical Boundary Conditions on Phase Diagrams of Epitaxial Ferroelectric Thin Films. *Phys. Rev. Lett.*, 80:1988–1991, 1998.

[25] M. Kawai, D. Kan, S. Isojima, H. Kurata, S. Isoda, S. Kimura, O. Sakata, and Y. Shimakawa. Deposition Rate Effect on Critical Thickness of $BaTiO_3$ Epitaxial Thin Film Grown on $SrTiO_3$ (001). *Mater. Res. Soc. Symp. Proc.*, 1034:K10–04, 2008.

Appendix A

Fit program

This appendix presents the *MatLab*© program used to determine the thickness and out-of-plane lattice parameter of thin films and superlattices. In the following, the main program is shown which handels the inputs and calculats the polynomial approximation of the *atomic structure factor* for each material. Input parameter are the number of materials nm, the A- and B- side atoms tA and tB, the c-axis value c, the number of unit cells per layer N and the number of superlattice periods MM.

```
%CALCULATED X-R DIFFRACTED INTENSITY ON SUPERLATTICES BASED ON
%                    MANY DIFFERENT FERRO.
%*************************************************************
%*************************************************************
%----------------------VARIABLES
global A B O x MM TA L TTA iTTAlim1 nm norm ldata;
iTTAlim1=0;
%----------------------INPUTS:
nm=input('Number of different materials involved : ');

tA=zeros(nm,1); tB=zeros(nm,1);
c=zeros(nm,1); N=zeros(nm,1);

for j=1:nm
    materialnumber=j
    tA(j)=input('A-atoms (Pb-type 1, Sr-type 2, Ba-type 3) : ');
    tB(j)=input('B-atoms (Ti-type 1, Ru-type 2) : ');
    c(j)=input('c axis parameter : ');
    N(j)=input('number of unit cells : ');
end;

if nm==1
    MM=1;
```

```
else
    MM=input('number of superlattice periods : ');
end;
%------LOAD EXPERIMANTAL DATA
load data.dat;
data=data;
norm=input('normalization factor for data : ');
data(:,2)=data(:,2)/norm;
%------PLOT RANGE
TTAmin=data(1,1);
ldata=length(data);
TTAmax=data(ldata,1);
TTAstep=0.001;

TTA=(TTAmin:TTAstep:TTAmax)';
[L,C]=size(TTA);
A=zeros(L,nm); B=zeros(L,nm); O=zeros(L,1);
TA=zeros(L,1); x=zeros(L,1);
TA=0.5*TTA*pi/180;
x=sin(TA)/1.5406;

%ATOMIC STRUCTURE FACTORS FROM TABLES IN POLINOMIAL
%APROXIMATION:
for j=1:nm,
    if tA(j)==1       %Pb
        A(:,j)=82*(1-0.473*x-20.84541*x.^2+99.69372*x.^3
        -223.54418*x.^4+287.35679*x.^5-222.30334*x.^6
        +102.18889*x.^7-25.70329*x.^8+2.7234*x.^9);
    elseif tA(j)==2   %Sr
        A(:,j)=38*(1-4.48384*x+1.50832*x.^2+44.32046*x.^3
        -149.03945*x.^4+230.90344*x.^5-199.86529*x.^6
        +99.13916*x.^7-26.35246*x.^8+2.91192*x.^9);
    elseif tA(j)==3   %Ba
        A(:,j)=56*(1-4.00272*x-2.26282*x.^2+58.11014*x.^3
        -177.67114*x.^4+266.80001*x.^5-227.47231*x.^6
        +111.85731*x.^7-29.56998*x.^8+3.25535*x.^9);
    end;
    if tB(j)==1       %Ti
        B(:,j)=22*(1-2.31679*x-17.71829*x.^2+117.81669*x.^3
        -302.97547*x.^4+422.61891*x.^5-345.38044*x.^6
        +165.13263*x.^7-42.77782*x.^8+4.96778*x.^9);
    elseif tB(j)==2   %Ru
        B(:,j)=44*(1-0.92972*x-18.59341*x.^2+93.8134*x.^3
        -214.77536*x.^4+279.87987*x.^5-218.81936*x.^6
        +101.45915*x.^7-25.70417*x.^8+2.74011*x.^9);
    end;
O=8.0*(1+.36093*x-16.97321*x.^2+56.02403*x.^3-92.92582*x.^4
    +90.0941*x.^5-56.77212*x.^6+21.36177*x.^7-4.4952*x.^8
    +0.40563*x.^9);
```

```
73 end;
74 %%-------------------------------------------------------------------
75
76 coef=[c,N];
77 int=Intensity(coef);     %calculate Intensity
78 Lambda=sum(N.*c)         %indicates the value of LA
79
80 %----------------------GRAPHIC OUTPUT:
81 subplot(2,1,1);
82 semilogy(TTA,int,'-g',data(:,1),data(:,2),'-r');
83 axis([TTAmin TTAmax 0.00001 1]);
84 xlabel('2Theta [Deg]');
85 ylabel('Intensity [A.U.]');
86 subplot(2,1,2);
87 plot(TTA,int,'-g',data(:,1),data(:,2),'-r');
88 axis([TTAmin TTAmax 0.00001 1]);
89 xlabel('2Theta [Deg]');
90 ylabel('Intensity [A.U.]');
91 %-------------------------------------------------------------------
```

The intensity is calculated by the function *Intensity(coef)* in the main program:

```
1  %calculates the x-ray intensity of the superlattice
2
3  function y=Intensity(coefy)
4
5  global A B O x MM TA L nm;
6  c=coefy(1:nm); N=coefy(nm+1:2*nm);
7  LA=sum(N.*c);   %modulation wavelength of the superlattice
8
9  %-----------------------------------------
10 FUC=zeros(L,1);
11 Δ=0;
12
13 for j=1:nm,
14     FF=zeros(nm,1); f=zeros(nm,1);
15     %-------one unit cell
16     f=(A(:,j)+O)+(B(:,j)+2*O).*exp(i*2*pi*x*c(j));
17
18     %-------one layer
19     FF=f.*sin(2*pi*x*N(j)*c(j))./sin(2*pi*x*c(j));
20
21     if j≠1,
22         Δ=Δ+c(j-1)*N(j-1);
23     end;
24     FUC=FUC+FF.*exp(i*Δ*4*pi*x);
25 end;          %to check UNIT CELL STRUCTURE FACTOR
26
```

```
27 %———————————INTERFERENCE FUNCTION FOR MM PERIODS
28 FINT=sin(MM*2*LA*x*pi)./sin(2*LA*x*pi);
29
30 %LORENZ—POLARIZATION FACTOR * ABSORPTION CORRECTION,
31 %   cf. PRB45(16)9292(1992)
32 LPA=(1+(cos(2*TA)).^2)./sin(2*TA).*(1—exp(—2*1.52*10^(—5)*
33     *MM*LA./sin(TA)));
34
35 %———————————INTENSITY
36 y=(abs(FUC.*FINT)).^2.*LPA;
37
38 %———————————RENORMALISATION OF THE INTENSITY:
39 y=y/max(y);
```